


Article

The Study of Reverse Water Gas Shift Reaction Activity over Different Interfaces: The Design of Cu-Plate ZnO Model Catalysts

Jinjun Wen ¹, Chunlei Huang ¹, Yuhai Sun ¹ , Long Liang ¹, Yudong Zhang ¹, Yujun Zhang ¹, Mingli Fu ^{1,2}, Junliang Wu ^{1,2}, Limin Chen ^{1,2,*} and Daiqi Ye ^{1,2}

¹ Guangdong Provincial Key Laboratory of Atmospheric Environment and Pollution Control, School of Environment and Energy, South China University of Technology, Guangzhou 510006, China; mrwenjj@163.com (J.W.); h13771888573@163.com (C.H.); sunyuhai1110@163.com (Y.S.); ll2235653307@163.com (L.L.); zyd1536872623@163.com (Y.Z.); zhangyujun34@163.com (Y.Z.); mlfu@scut.edu.cn (M.F.); ppjl@scut.edu.cn (J.W.); cedqye@scut.edu.cn (D.Y.)

² National Engineering Laboratory for VOCs Pollution Control Technology and Equipment, South China University of Technology, Guangzhou 510006, China

* Correspondence: liminchen@scut.edu.cn; Tel.: +86-20-3938-0508

Received: 29 March 2020; Accepted: 6 May 2020; Published: 12 May 2020



Abstract: CO₂ hydrogenation to methanol is one of the main and valuable catalytic reactions applied on Cu/ZnO-based catalysts; the interface formed through Zn migration from ZnO support to the surface of Cu nanoparticle (ZnOx-Cu NP-ZnO) has been reported to account for methanol synthesis from CO₂ hydrogenation. However, the accompanied reverse water gas shift (RWGS) reaction significantly decreases methanol selectivity and deactivates catalysts soon. Inhibition of RWGS is thus of great importance to afford high yield of methanol. The clear understanding of the reactivity of RWGS reaction on both the direct contact Cu-ZnO interface and ZnOx-Cu NP-ZnO interface is essential to reveal the low methanol selectivity in CO₂ hydrogenation to methanol and look for efficient catalysts for RWGS reaction. Cu doped plate ZnO (ZnO:xCu) model catalysts were prepared through a hydrothermal method to simulate direct contact Cu-ZnO interface and plate ZnO supported 1 wt % Cu (1Cu/ZnO) catalyst was prepared by wet impregnation for comparison in RWGS reaction. Electron paramagnetic resonance (EPR), XRD, SEM, Raman, hydrogen temperature-programmed reduction (H₂-TPR) and CO₂ temperature-programmed desorption (CO₂-TPD) were employed to characterize these catalysts. The characterization results confirmed that Cu incorporated into ZnO lattice and finally formed direct contact Cu-ZnO interface after H₂ reduction. The catalytic performance revealed that direct contact Cu-ZnO interface displays inferior RWGS reaction reactivity at reaction temperature lower than 500 °C, compared with the ZnOx-Cu NP-ZnO interface; however, it is more stable at reaction temperature higher than 500 °C, enables ZnO:xCu model catalysts superior catalytic activity to that of 1Cu/ZnO. This finding will facilitate the designing of robust and efficient catalysts for both CO₂ hydrogenation to methanol and RWGS reactions.

Keywords: reverse water-gas shift reaction; CO₂ hydrogenation to methanol; Cu doping; direct contact Cu-ZnO interface; ZnOx-Cu NP-ZnO interface

1. Introduction

In the recent years, climate change and ocean acidification resulting from the emission of greenhouse gases have received widespread attention in the environmental and energy fields [1–3]. Consequently, the utilization and conversion of CO₂ to valuable chemicals have been proposed to alleviate CO₂ emission [4,5]. Among them, CO₂ hydrogenation to methanol is a promising way to

reduce the emission and make the utilization of CO₂. Methanol is an excellent commodity chemical, served as an alternative fuel and feedstock in the chemical industry [6]. Considering the sources of hydrogen, it also can be produced through renewable energies, such as solar energy, wind power, hydropower and biomass. However, methanol formation always accompanies with CO formation, known as the reverse water gas shift (RWGS) reaction, which significantly decreases methanol selectivity. Furthermore, RWGS reaction is a critical intermediate step for Sabatier reaction and Fischer–Tropsch synthesis (FTS), participating in a pivotal process of transforming the CO₂ feedstock into chemicals or hydrocarbon fuels through syngas process, which is significant in the storage of renewable energy. Therefore, RWGS reaction also has attracted more and more attention.

Cu/ZnO-based catalysts are typical catalysts applied in industrial methanol synthesis from syngas hydrogenation and water gas shift (WGS) reaction [7–11]. In addition, Cu/ZnO-based catalysts are still the most efficient catalysts for methanol synthesis from CO₂ hydrogenation compared with other reported catalysts [6,12]. Therefore, the clear understanding of the catalyst structure is critical in improving the catalytic performance of the above three reactions. It has been reported that the superior catalytic performance is due to the synergy effects originating from the strong metal-support interactions (SMSI) between Cu and ZnO [13–15]. Correspondingly, the synergy effects between Cu and ZnO support on catalytic performance were investigated. Although abundant publications reported that the catalytic activity could be promoted by tuning the Cu–ZnO synergy effects, such as optimizing ZnO morphology, Cu nanoparticle morphology, size, the introduction of additives, etc. [9,16–19], the maximum methanol yield seldom exceeded 14.0% with methanol selectivity about 60.3% over Cu–ZnO based catalysts under the typical reaction conditions (H₂/CO₂ = 3/1, 3 MPa, 2240 h⁻¹, 230 °C) [20].

Recent publications further reveal that SMSIs between Cu and ZnO will induce ZnOx migration from bulk ZnO support to the surface of Cu nanoparticle during activation in H₂ and the coverage of Zn species is essential to methanol formation [12,21–23]. Then, it can be speculated that there are both direct contact Cu–ZnO interface and migrated ZnOx covered Cu nanoparticle interface (ZnOx–Cu NP–ZnO) over the supported Cu–ZnO based catalysts. Furthermore, surface science exploration and DFT simulation disclosed that ZnOx–Cu NP–ZnO interface exhibits apparent higher reactivity for methanol formation than that of direct contact Cu–ZnO interface [23–25]. This valuable finding stimulates us to think about the reactivity of RWGS reaction on these two interfaces; then, the further fate of the produced CO and the origin of the low methanol selectivity (methanol production from CO₂ hydrogenation) over Cu–ZnO based catalysts.

The purpose of this research is to elucidate the reactivity of RWGS reaction on both direct contact Cu–ZnO interface and ZnOx–Cu NP–ZnO interface, and then facilitates to uncover the origin of the low methanol selectivity during CO₂ hydrogenation. Thus, it is very meaningful in understanding the reactivity of RWGS and methanol selectivity on both Cu–ZnO interfaces. However, it is difficult to differentiate these two interfaces from real supported catalysts and their corresponding reactivity; on the other hand, there are material gap and pressure gap for surface science research and DFT simulation, although both can provide clear micro structure information. Thus, powder model catalysts should be designed, especially for direct contact Cu–ZnO interface simulation. Campbell et al. [24] investigated the methanol synthesis reactivity on both Cu/ZnO (000 $\bar{1}$) and ZnOx/Cu (111) catalyst models prepared through depositing a monolayer Cu on ZnO (000 $\bar{1}$) surface and a monolayer ZnOx on Cu (111) crystal, respectively. They reported that Cu bonded directly to the ZnO substrate to form stable direct contact Cu–ZnO interface over Cu/ZnO (000 $\bar{1}$) catalyst model while the latter formed ZnOx–Cu interface. Thus, it is reasonable to construct direct contact Cu–ZnO interface through doping ZnO with Cu; accordingly, traditional supported catalysts can simulate both types of Cu–ZnO interfaces.

The 1 wt % Cu/plate ZnO model catalyst has been well investigated for CO₂ hydrogenation to methanol in our previous publications [26,27]. It has revealed that this model catalyst consists of both direct contact Cu–ZnO interface and ZnOx–Cu NP–ZnO interface, as expected. Our previous research indicates that plate ZnO is flexible to be doped with rare earth metals and transition metals,

which inspires us to construct Cu doped plate ZnO as a model catalyst to simulate the direct contact Cu-ZnO interface [28–31]. In order to clearly investigate the reactivity of RWGS reaction on the direct contact Cu-ZnO interface, a series of Cu doped plate ZnO (ZnO:X) have been prepared including the samples with exceeding doping limit. The reactivity over both plate ZnO:X and Cu/plate ZnO model catalysts were evaluated and their structures were confirmed through SEM, electron paramagnetic resonance (EPR), XRD and Raman characterizations. Finally, the RWGS reaction performance over direct contact Cu-ZnO interface and ZnO_x-Cu-ZnO interface was comparatively explored and discussed.

2. Results and Discussion

2.1. Catalyst Characterization

Figure S1 presented SEM images of the pristine plate ZnO and 1Cu/ZnO catalyst after reduction. The pure plate ZnO has regular plate-like morphology and relatively large particle size. For 1Cu/ZnO sample after reduction, Cu nanoparticles were highly dispersed on the plate ZnO and the morphology of the support was kept. Accordingly, Figure 1 displayed SEM images of ZnO:XCu model catalysts after reduction. All samples exhibited plate-like morphology, indicating that plate ZnO model catalyst morphology was not changed during Cu doping while the size especially the thickness decreased significantly from 1.5 μm (Figure S1) to submicrometer. This means it is not realistic to use HRTEM related techniques to investigate their fine structures. Thus, the elemental mappings of ZnO:XCu model catalysts were also presented as shown in Figure 1. It is obvious that although no Cu particle can be clearly observed on the plate ZnO surface, Cu element distribution can be detected in EDS mapping. This suggests that Cu may be incorporated into the bulk ZnO. However, when the amount of Cu reached 6.5 wt % as shown in Figure 1e, a few Cu nanoparticles can be observed on plate ZnO surface. This reveals that the maximum doping amount of Cu should be lower than 6.5 wt %. Therefore, these data indicate that all samples should have formed the direct contact Cu-ZnO interface; the ZnO:6.5Cu sample should form additional ZnO_x-Cu NP-ZnO interface caused by ZnO_x migration during the reduction in H₂.

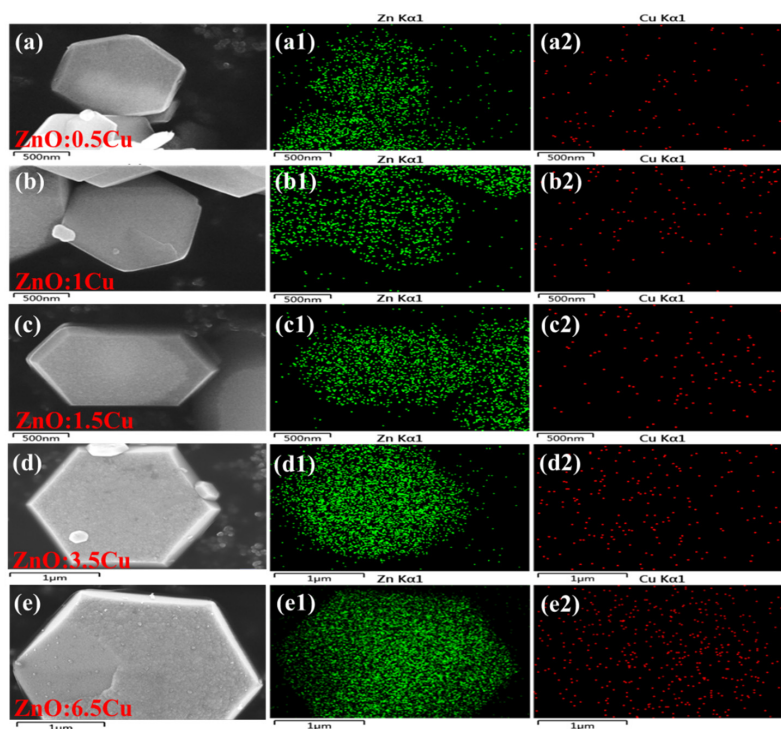


Figure 1. SEM images and corresponding elemental mapping of the reduced catalysts: ZnO:0.5Cu (a–a2), ZnO:1Cu (b–b2), ZnO:1.5Cu (c–c2), ZnO:3.5Cu (d–d2) and ZnO:6.5Cu (e–e2).

EPR is sensitive to the paramagnetic defects and the coordination of doped Cu^{2+} ions in ZnO. Figure 2 displayed the EPR profiles of the as-synthesized pristine plate ZnO and Cu doped plate ZnO. For all catalysts, the resonance at $g = 1.953$ is attributed to the shallow donor centers caused by the interstitial Zn (Zn_i) and surface O vacancy (V_o) [32–34]. Compared with the pristine plate ZnO, this peak intensity of plate ZnO:Cu samples was relatively weaker and decreased with the increasing of Cu doping amount. This phenomenon implies the incorporation of Cu into ZnO metal framework and the substitution of Zn_i [35]. Meanwhile, the anisotropic hyperfine structure was observed in Cu containing plate ZnO samples. The resonances parameter $g_{\parallel} = 2.384$ and $g_{\perp} = 2.095$ indicate that the Cu^{2+} replaces the cation sites of ZnO [36–40]. Furthermore, $g_{\parallel} > g_{\perp} > g_e = 2.002$ unveils that Cu^{2+} ions are subjected to tetragonally elongated distortion and in a ligand field of tetragonal symmetry, coordinated by six ligand atoms [32,41]. However, when the amount of Cu reached 3.5 wt %, the anisotropic hyperfine structure was not obvious enough or even disappeared, which is attributed to the increase of the long-range dipolar interaction between Cu^{2+} ions along the increase of the Cu doping amount [37,42,43]. Thus, the EPR results confirm that Cu^{2+} was successfully doped into the ZnO lattice.

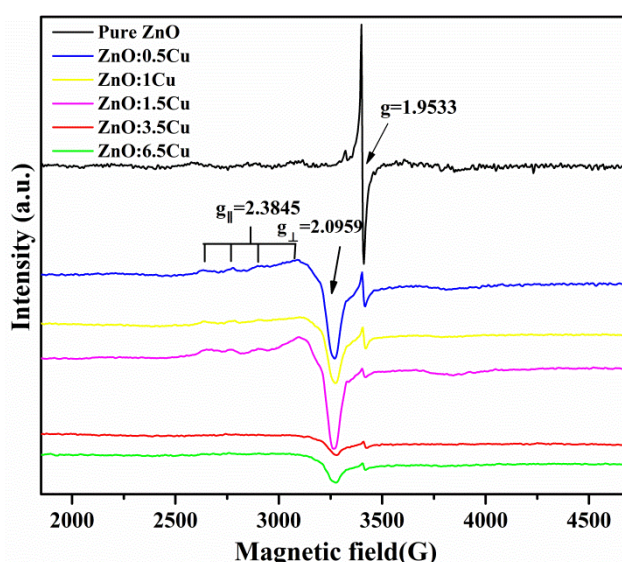


Figure 2. Electron paramagnetic resonance (EPR) profiles of the as-synthesized pure plate ZnO and ZnO:XCu, X = 0.5, 1.0, 1.5, 3.5, 6.5.

The XRD patterns of the calcined pristine ZnO and ZnO:XCu samples were presented in Figure 3a. The diffraction peaks located at $2\theta = 31.74, 34.38, 36.21, 47.48, 56.53, 62.78, 66.30, 67.87, 69.00, 72.46$ and 76.87° are corresponded to the diffraction from (100), (002), (101), (102), (110), (103), (200), (112), (201), (004) and (202) planes of the hexagonal wurtzite structure (JCPDS Card No. 89-1397), respectively. The diffraction pattern of all samples showed the orientation prefers along (101) plane and the hexagonal wurtzite structure was kept during doping. However, when the amount of Cu achieved 3.5 wt %, another two diffraction peaks appeared at approximately $2\theta = 42.3$ and 43.3° , attributed to the diffraction of Cu_2O (200) and Cu (111), respectively. The appearance of Cu_2O and elemental Cu may be due to the auto-reduction of the Cu^{2+} ions adsorbed on the surface of plate ZnO during the calcination in oxygen-free environment [44]. Figure 3b displayed the enlarged diffraction peak of Cu doped ZnO (002) plane, which clearly showed a left shift and an intensity decrease of this peak with a rise in Cu concentration. Such kinds of XRD diffraction peak shift and intensity decrease depend upon the preparation conditions like doping procedures and have been studied extensively in Cu doped ZnO [30,45]. However, ZnO:6.5Cu sample showed intensity increase and right shift of the (002) diffraction peak. Such a shift at higher Cu concentration is consistent with previous reported results on Cu doped ZnO film, but the reasons are not clear [46]. The XRD patterns of the reduced ZnO:XCu

samples were shown in Figure S2. After reduction, Cu (111) phase can be observed over ZnO:3.5Cu and ZnO:6.5Cu samples except ZnO diffraction. Both EPR and XRD results demonstrate the doping of Cu into bulk plate ZnO; the direct contact Cu-ZnO interface will be produced after reduction in H₂.

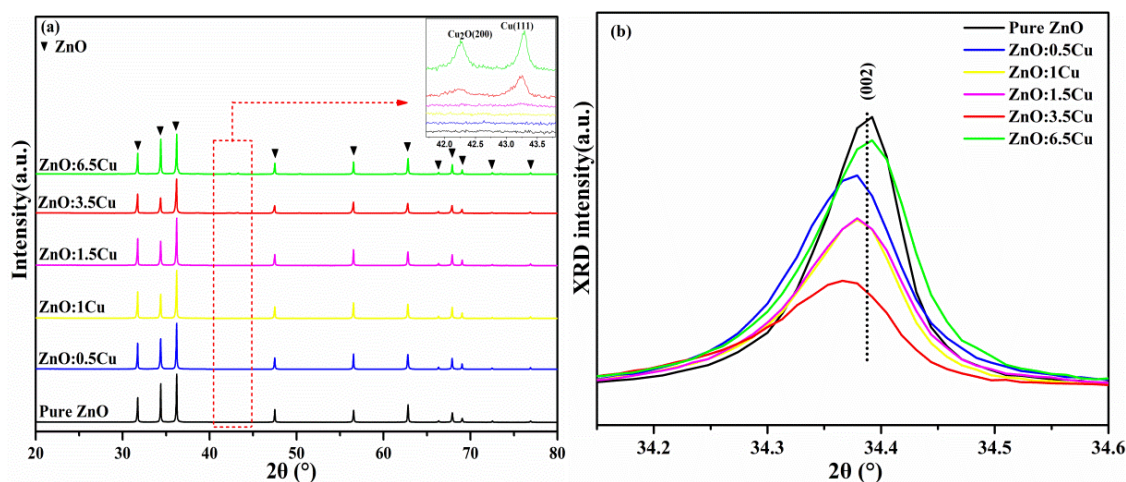


Figure 3. XRD patterns of the calcined ZnO:XCu model catalysts (a) and the diffraction peak of the ZnO (002) plane (b).

Raman spectroscopy is an effective technique to investigate structure changes induced by defects. The Raman spectra of the calcined plate ZnO and ZnO:XCu in the wave number range of 200–800 cm⁻¹ were shown in Figure 4. The Raman peaks of pristine plate ZnO located at 332, 380, 438 and 582 cm⁻¹ corresponded to E₂^{high}-E₂^{low}, A₁(TO), E₂^{high} and E₁(LO), respectively. E₂^{high}-E₂^{low} and A₁(TO) are attributed to a second-order phonon and first-order phonon, respectively. The Raman mode of E₂^{high} is assigned to the oxygen vibration. The E₁(LO) mode originates from second-order Raman scattering, which is affected by impurities and/or defects (Zn_i, V_o) [47]. It can be clearly seen from the inset of Figure 4 that the E₂^{high} mode in ZnO:XCu exhibited red shift from 439 to 428 cm⁻¹ compared with that of pristine ZnO. Furthermore, the E₂^{high} showed a significant intensity decrease and line shape broadness along with the increase of Cu doping. The red shift, weakening and broadening of E₂^{high} are the consequence of the defect formation and local lattice distortions caused by Cu doping [31,48]. Similar characteristics can be found in the previous publications [47,48]. This indicates the incorporation of Cu into ZnO, in good agreement with EPR and XRD results. The intensity ratios of E₁(LO) to E₂^{high} were calculated as an indicator to reflect the corresponding defect concentrations of ZnO:XCu after the doping by the phonon confinement model (PCM) [47,49]. The wavenumber of E₂^{high} and the intensity ratio of E₁(LO) to E₂^{high} were listed in Table 1. The value of the intensity ratio of E₁(LO) to E₂^{high} increased in the order of ZnO < ZnO:0.5Cu < ZnO:1Cu < ZnO:1.5Cu < ZnO:3.5Cu < ZnO:6.5Cu, increasing along with Cu amount. Then, the correlation between the intensity ratio of E₁(LO) to E₂^{high} and the Cu content were displayed in Figure S3. With the increase of Cu amount, ZnO:XCu model catalysts possessed more structure defects. The defect amounts of catalysts kept good linear with the Cu doping amount, except for the ZnO:6.5Cu sample although it has the highest value, indicating the non-linear increase of defects. Moreover, the Raman spectra and the intensity ratio of E₁(LO) to E₂^{high} for the reduced samples were presented in Figure S4 and Table S1, respectively. More defects can be obtained due to oxygen vacancy formation during the reduction in H₂. However, it should be noted that the increment of the intensity ratio of E₁(LO) to E₂^{high} was gradually getting smaller along with Cu increase and there was hardly any increase for ZnO:6.5Cu after reduction. This indicates that this sample has quite different defect distribution compared with other samples with low Cu concentration.

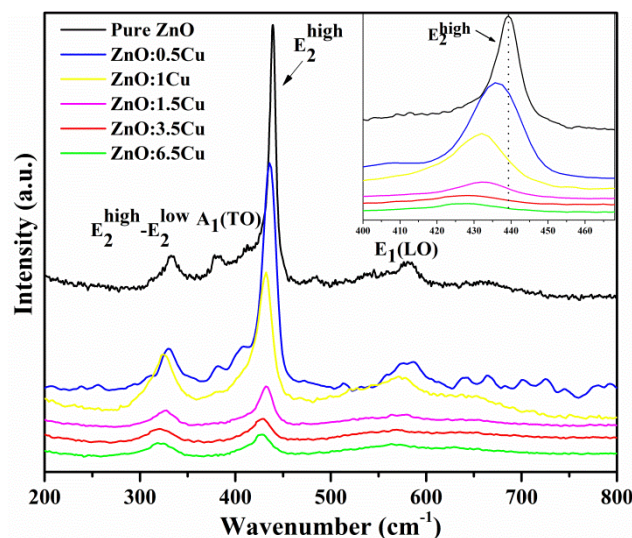


Figure 4. Raman spectra of the calcined pristine ZnO and ZnO:XCu model catalysts, X = 0.5, 1.0, 1.5, 3.5, 6.5.

Table 1. The wave number of E_2^{high} and intensity ratios of $E_1(LO)$ to E_2^{high} for the calcined pristine ZnO and ZnO:XCu model catalysts.

Samples	ZnO	ZnO:0.5Cu	ZnO:1Cu	ZnO:1.5Cu	ZnO:3.5Cu	ZnO:6.5Cu
E_2^{high} (cm ⁻¹)	439	436	432	432	428	428
$E_1(LO)/E_2^{high}$	0.09	0.13	0.22	0.27	0.45	0.53

The hydrogen temperature-programmed reduction (H_2 -TPR) profiles of various Cu doped ZnO were presented in Figure 5 in order to determine the reduction process of Cu species. Three reduction peaks can be deconvoluted, the reduction temperature range of 130–145 °C, 150–160 °C and 170–180 °C, corresponded to α , β and γ peak, respectively. The α peak was ascribed to the reduction of $Cu^{2+} \rightarrow Cu^+$ and further reduction to Cu^0 [36,50]. In addition, this behavior suggests a certain interaction between the incorporated Cu and ZnO support [51]. The β peak was attributed to the reduction of Cu^+ to Cu^0 due to the unreacted Cu^+ from the two-step reduction process of dopant Cu^{2+} [36]. Compared to the lower doping samples, ZnO:3.5Cu and ZnO:6.5Cu both have a unique H_2 consumption peak, γ , in the temperature region of 170–180 °C, which should be assigned as the reduction of Cu_2O according to XRD results. These results indicate that all Cu species can be reduced to Cu^0 to form the direct contact Cu-ZnO interface.

Interestingly, there were two negative peaks displayed in the temperature range of 300–450 °C and 550–650 °C, respectively. The higher temperature negative peak can be attributed to hydrogen release from bulk ZnO support according to the H_2 temperature-programmed desorption (H_2 -TPD) of pristine plate ZnO and ZnO:1Cu after reduction in H_2 at 300 °C without H_2 adsorption treatment, as displayed in Figures S5 and S6, respectively. Compared to the pure ZnO, the additional lower temperature negative peak probably should be related to Cu doping. In addition, Chen et al. [52] reported that the active metallic atom could dissociate molecular hydrogen into atomic hydrogen species and then migrate to the defects of support. Therefore, the negative peak of ZnO:XCu catalysts at much lower temperature can be postulated to the desorption of the dissociatively adsorbed hydrogen species on the lattice defects of ZnO support due to the spill over from the reduced Cu dopant.

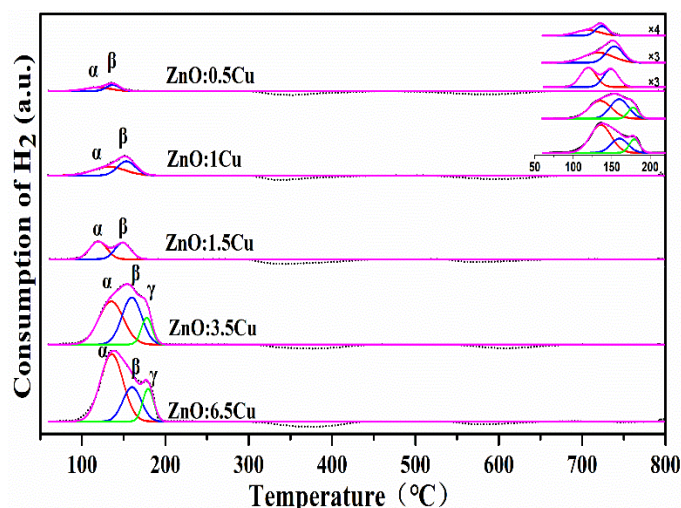


Figure 5. Hydrogen temperature-programmed reduction (H_2 -TPR) profiles of ZnO:XCu model catalysts, X = 0.5, 1.0, 1.5, 3.5, 6.5.

CO_2 -TPD profiles of ZnO:XCu model catalysts were shown in Figure 6 to acquire the CO_2 adsorption capabilities. Four desorption peaks can be observed approximately at 84, 371, 429 and 662 °C, denoted as α , β_1 , β_2 and γ , respectively. In general, the four desorption peaks were corresponded to the adsorption on weak basic sites (α peak), moderate basic sites (β_1 , β_2 peak) and strong basic sites (γ peak), which were associated with the hydroxy group, metal-oxygen pairs and low coordination oxygen atoms, respectively [53,54]. In comparisons, the CO_2 -TPD profile of the pristine plate ZnO was also displayed in Figure 6. However, α peak was absent in the patterns of pristine plate ZnO. The presence of the α peak for all Cu doped ZnO samples indicates that the addition of Cu can improve the CO_2 adsorption ability on catalyst surface. The desorption peak temperature and respective peak area of the ZnO:XCu and 1Cu/ZnO (Figure S7) model catalysts were listed in Table 2. The total peak area of β_1 plus β_2 of the pristine plate ZnO was very small and hardly exhibited any activity. The desorption from peak β_1 and β_2 over ZnO:XCu model catalysts increased along with the amount of Cu, indicating that the incorporation of Cu prompts CO_2 adsorption and activation. The increasing desorption amounts of CO_2 from medium basic sites may be attributed to the electronic promotion effects of Cu dopant, more defect sites on the Cu-ZnO interface, providing additional active sites to adsorb CO_2 . Although Raman result demonstrates that ZnO:6.5Cu had more defects compared to that of ZnO:3.5Cu, it exhibited less CO_2 desorption. This is because that the ZnO:6.5Cu sample has quite different defect distribution mode compared with other ZnO:XCu model catalysts; furthermore, only oxygen vacancies are generally considered to be responsible for CO_2 adsorption other than intrinsic defects caused by lattice distortion. Besides, considering about the high CO_2 desorption from 1Cu/ZnO, the lower desorption from ZnO:6.5Cu sample should be also due to small amount of Cu NPs on the doped plate ZnO surface and the different electronic properties between the doped ZnO and pure ZnO surfaces, according to the previous publications [55]. Thus, although ZnO:6.5Cu sample had a large quantity of defects with a few Cu NPs on doped ZnO surface, it still showed comparable CO_2 desorption to that of ZnO:1.5Cu.

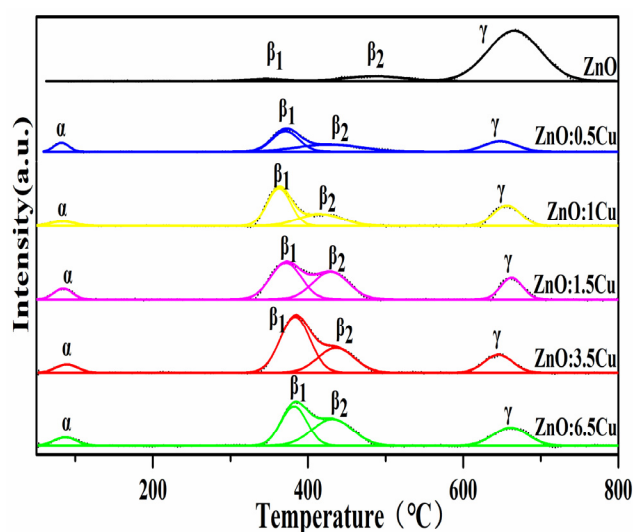


Figure 6. CO₂ temperature-programmed desorption (CO₂-TPD) profiles of the reduced pure ZnO and ZnO:XCu model catalysts, X = 0.5, 1.0, 1.5, 3.5, 6.5.

Table 2. CO₂ desorption capabilities of the reduced pure ZnO and ZnO:XCu model catalysts.

Samples	CO ₂ Desorption Amount ($\mu\text{mol}\cdot\text{g}^{-1}$), Temperature				Total ($\beta_1 + \beta_2$)
	α , T (°C)	β_1 , T (°C)	β_2 , T (°C)	γ , T (°C)	
ZnO	-	0.39 (342)	1.06 (486)	8.46 (665)	1.45
ZnO:0.5Cu	0.40 (82)	1.65 (371)	1.37 (427)	1.03 (648)	3.02
ZnO:1Cu	0.36 (83)	2.73 (363)	1.64 (416)	1.74 (656)	4.37
ZnO:1.5Cu	0.63 (84)	3.46 (371)	3.02 (429)	1.45 (662)	6.48
ZnO:3.5Cu	0.55 (89)	5.09 (383)	2.76 (436)	1.56 (645)	7.85
ZnO:6.5Cu	0.58 (89)	3.18 (382)	3.31 (431)	1.95 (661)	6.49
1Cu/ZnO	0.88 (90)	4.34 (322)	4.80 (392)	9.48 (662)	9.14

2.2. Catalytic Performance

The catalytic performance of 1Cu/ZnO and ZnO:XCu samples was evaluated. For all samples, higher CO₂ conversion can be obtained at higher reaction temperature as shown in Figure 7a. The doping of Cu can significantly improve the catalytic activity and the ZnO:3.5Cu sample exhibited the highest CO₂ conversion for RWGS reaction. With a further increase in the amount of Cu, the activity of ZnO:6.5Cu was suppressed and even lower than that of ZnO:3.5Cu at 550 °C. This indicates that there exists an optimum copper doping amount and a further increase in the amount of Cu would decrease the catalytic activity. Furthermore, in order to further understand the reactivity of direct contact Cu-ZnO interface on RWGS reaction, the CO formation rate per catalyst weight (R_w) on the investigated catalysts as a function of Cu amount at 450 °C were illustrated in Figure 7b. As shown, when the amount of Cu less than 3.5 wt %, CO formation rate by catalyst weight increased along with the Cu doping amount and presented almost linear correlation. This implies that higher Cu doping is beneficial to RWGS reaction. Compared with all ZnO:XCu catalysts, it is clear that 1Cu/ZnO exhibits the superior catalytic reactivity at 450 °C; however, when the reaction temperature higher than 500 °C, it is significantly lower than that of ZnO:XCu model catalysts.

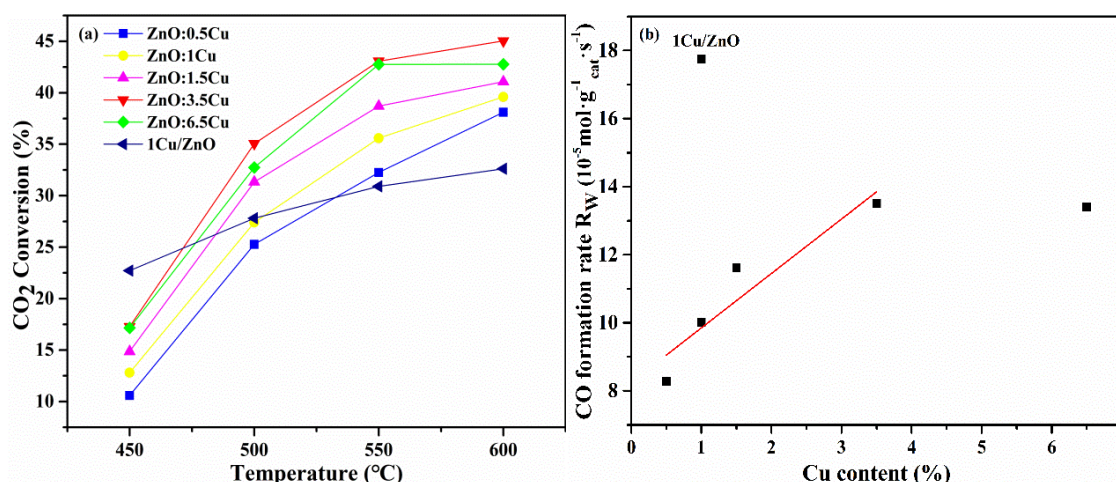


Figure 7. Catalytic performance of 1Cu/ZnO and ZnO:XCu model catalysts, X = 0.5, 1.0, 1.5, 3.5, 6.5 (a) and R_W as a function of the amount of Cu for the reverse water gas shift (RWGS) reaction at 450 °C (b).

2.3. Discussion

2.3.1. The RWGS Reactivity over Different Cu-ZnO Interfaces

The surface basic sites are pivotal to the RWGS reaction. According to the previous publications, the introduction of transition metal dopants (Cu^{2+} , Ni^{2+} , Fe^{2+} etc.) will change the basicity of the host metal oxides, then modifying the adsorption capacity and strength of acidic CO_2 [56–58]. Here, the desorption from medium basic sites increase along with the increase of Cu doping; however, when the amount of Cu reached 6.5 wt %, it was only close to that of ZnO:1.5Cu according to CO_2 -TPD. Then, the relationship between R_{SSA} and CO_2 desorption density (based on the surface area) from the medium basic sites was displayed in Figure 8 and the corresponding specific surface area of all samples was listed in Table S2. Figure 8 clearly demonstrates that the higher density of the moderately adsorbed carbon species leads to higher R_{SSA} and plays important roles in CO formation. Interestingly, ZnO:6.5Cu has higher R_{SSA} than that of ZnO:1.5Cu but with similar amount of carbon species desorption from the medium basic sites. EPR results indicate that doped Cu^{2+} mainly replace lattice Zn^{2+} sites and interstitial sites (Zn_i), while SEM and XRD characterization demonstrate the appearance of some Cu NPs on the surface of plate ZnO over ZnO:6.5Cu sample. Besides, it is widely accepted that the ZnOx will migrate from bulk ZnO support to the surface of Cu NPs to form ZnOx-Cu-ZnO interface during reduction in H_2 [12,22], which should account for the peculiar CO_2 adsorption behavior of ZnO:6.5Cu sample. Therefore, the higher RWGS reactivity of ZnO:6.5Cu compared to ZnO:1.5Cu should be due to the formation of ZnOx-Cu NP-ZnO interface on ZnO:6.5Cu. This means ZnOx-Cu NP-ZnO interface also displays apparent RWGS reactivity.

Based on our previous publications [26,27], the 1Cu/ZnO model catalyst has both the direct contact Cu-ZnO interface and ZnOx-Cu NP-ZnO interface. Here, the lower doped ZnO:XCu model catalysts only have the direct contact Cu-ZnO interface. Then, in order to further disclose the RWGS reactivity over different Cu-ZnO interfaces, the catalytic performance of the 1Cu/ZnO model catalyst was also presented in Figure 8. It is striking that R_{SSA} (based on the SSA of ZnO plate) is far higher than that of all ZnO:XCu model catalysts. Furthermore, the slope of 1Cu/ZnO model catalyst is much steeper than that of all ZnO:XCu model catalysts, which means the adsorbed carbon species on the former model catalyst are more active than those adsorbed on the latter ones or the specific surface area of ZnOx-Cu NP-ZnO interface should be also included. Thus, the specific surface area of ZnOx-Cu NP-ZnO interface was counted to calculate the R_{SSA} , which was about $35.91 \mu\text{mol} \cdot \text{m}^{-2} \text{Cu/ZnO} \cdot \text{s}^{-1}$ according to the specific surface area of 1Cu/ZnO model catalyst ($4.94 \text{ m}^2 \cdot \text{g}^{-1} \text{cat}$). This value is still above that of all ZnO:XCu model catalysts. Among all ZnO:XCu model catalysts, ZnO:3.5Cu model catalyst displayed the highest R_{SSA} ($34.62 \mu\text{mol} \cdot \text{m}^{-2} \text{ZnO:Cu} \cdot \text{s}^{-1}$), which reflects the maximum CO formation rate over

the simulated direct contact Cu-ZnO interface. The specific surface areas of plate ZnO and 1Cu/ZnO model catalyst were 2.93 and $4.94 \text{ m}^2 \cdot \text{g}^{-1}_{\text{cat}}$, respectively; then it can be roughly estimated that the specific surface area of Cu NPs was around $2.01 \text{ m}^2_{\text{Cu}} \cdot \text{g}^{-1}_{\text{cat}}$. Considering R_{SSA} over 1Cu/ZnO model catalyst is $35.91 \text{ } \mu\text{mol} \cdot \text{m}^{-2}_{\text{Cu/ZnO}} \cdot \text{s}^{-1}$, then R_{SSA} over ZnOx-Cu NP-ZnO interface could be calculated about $37.80 \text{ } \mu\text{mol} \cdot \text{m}^{-2}_{\text{Cu}} \cdot \text{s}^{-1}$, which was still higher than that of the direct contact Cu-ZnO interface simulated by ZnO:3.5Cu model catalyst. Thus, the incorporation of Cu into bulk plate ZnO to form direct contact Cu-ZnO interface was beneficial to the RWGS reaction; however, the ZnOx-Cu NP-ZnO interface was more active for the reaction at low temperature.

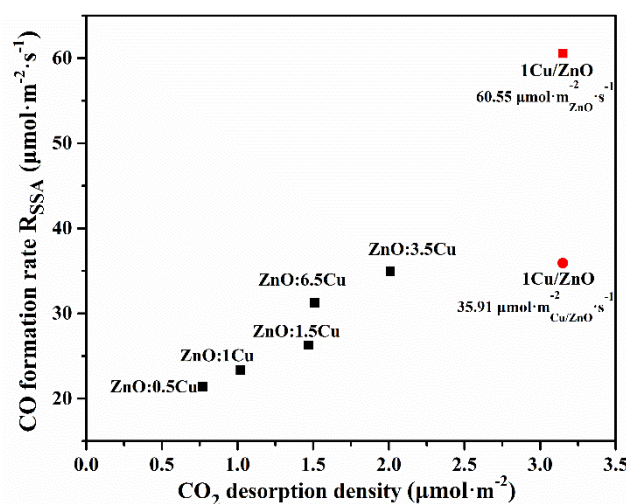


Figure 8. The relationship between CO formation rate R_{SSA} and CO_2 desorption density from peak ($\beta_1 + \beta_2$) at 450°C .

2.3.2. The RWGS Reaction Stability over Different Cu-ZnO Interfaces

Both the direct contact Cu-ZnO interface and ZnOx-Cu NP-ZnO interface were active for the RWGS reaction, the latter one was more active than the former at temperatures lower than 500°C . This is important in understanding the low methanol selectivity in CO_2 hydrogenation to methanol. However, the high temperature was essential to the RWGS reaction; thus, the catalytic performance of these samples at 600°C was comparatively investigated as displayed in Figure 9. As shown in Figure 9a, the initial CO_2 conversion of 1Cu/ZnO catalyst was lower than that of ZnO:1Cu, even lower than that of 0.5 wt % Cu doped plate ZnO at 600°C . Furthermore, the 1Cu/ZnO catalyst deactivated very quickly after 20 h measurement, and the activity of 1Cu/ZnO decreased 35.5%, as shown in Figure 9b. As known, Cu-based oxide catalysts are easily deactivated due to the sintering of surface Cu particles especially at high temperature [59,60]. This suggests that the specific surface area of the ZnOx-Cu NP-ZnO interface in the 1Cu/ZnO model catalyst will decrease, then lose activity quickly. In comparison, all ZnO:XCu samples possessed relatively stable catalytic performance especially when the doping amount was less than 3.5 wt %. These results mean that the aggregation and sintering of active Cu species in doped samples should not exist at high reaction temperature, improving the catalytic activity and stability. In order to exclude the influences of ZnOx-Cu NP-ZnO interface induced by Cu nanoparticle formation during the reaction evaluation, the SEM and XPS investigation of ZnO:1Cu model catalyst after RWGS stability evaluation were displayed in Figure S8 and Table S3, respectively. Although a slight deformation of plate morphology appeared, no Cu nanoparticle can be observed on the surface with only slight Cu/Zn ratio increase after the stability test, indicating no apparent Cu segregation during the reaction test. Accordingly, the activity loss over the ZnO:6.5Cu catalyst reached 35.14% after reaction for 20 h, similar to that of 1Cu/ZnO model catalyst. This further proved that the additional ZnOx-Cu NP-ZnO interface would impair the stability. According to the

above results, the direct contact Cu-ZnO interface is active for the RWGS reaction and more stable than that of the ZnOx-Cu NP-ZnO interface at high temperature.

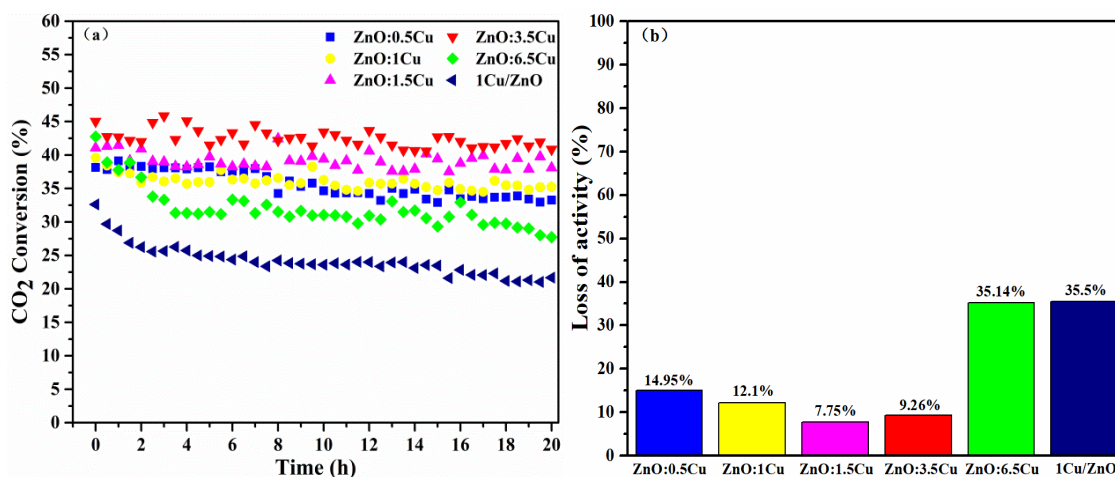


Figure 9. Stability test of Cu-ZnO model catalysts for the RWGS reaction at 600 °C (a) and catalytic activity loss percentage after reaction for 20 h (b).

3. Materials and Methods

3.1. Catalyst Preparation

3.1.1. Synthesis of Cu Doped Plate ZnO Catalysts

Cu doped plate ZnO model catalysts were synthesized by a hydrothermal method. Firstly, the required amounts of $\text{Cu}(\text{NO}_3)_2 \cdot 3\text{H}_2\text{O}$ (AR grade, Shanghai Aladdin) and zinc acetate dehydrate ($\text{Zn}(\text{CO}_2\text{CH}_3)_2$, 6.3 g, AR grade, Shanghai Aladdin) were dissolved in 60 mL deionized water, followed by addition of hexamethylenetetramine ($\text{C}_6\text{H}_{12}\text{N}_4$, 1.6 g, AR grade, Shanghai Aladdin). After 1 h vigorous magnetic stirring, the solution was transferred into a 100 mL Teflon-lined autoclave and maintained at 97 °C for 12 h. The resulted precipitate was collected after the autoclave cooled to room temperature, and then washed with deionized water and ethanol for several times, finally dried at 80 °C for 12 h and calcined at 350 °C for 3 h in pure N_2 . The final model catalysts with the doping amount were 0.5, 1.0, 1.5, 3.5 and 6.5 wt % determined by ICP analysis, denoted as ZnO:0.5Cu, ZnO:1Cu, ZnO:1.5Cu, ZnO:3.5Cu and ZnO:6.5Cu, respectively.

3.1.2. Synthesis of Cu/Plate ZnO Catalysts

The pristine plate ZnO was prepared according to ZnO:Cu preparation procedure without the addition of $\text{Cu}(\text{NO}_3)_2 \cdot 3\text{H}_2\text{O}$. 1 wt % Cu/plate ZnO model catalyst was prepared by the impregnation method. The required amount of $\text{Cu}(\text{CO}_2\text{CH}_3)_2 \cdot \text{H}_2\text{O}$ was dissolved in deionized water, then copper-containing solution was added to 2 g of plate ZnO support, and the slurry was stirred until dry. Finally, the sample was dried at 80 °C for 12 h in the oven, followed by calcination at 350 °C for 3 h in air. The obtained catalyst with Cu loading amount was 1 wt %, labeled as 1Cu/ZnO.

3.2. Characterization Technologies

Inductively coupled plasma (ICP) analysis was utilized to determine the actual copper amounts on an inductively coupled plasma-optical emission spectroscopy (ICP-AES, Thermo Scientific FLASH 2000). Scanning electron microscopy (SEM) images and energy dispersive X-ray spectroscopy (EDS) was obtained on a scanning electron microscope (Carl Zeiss Merlin, Germany).

Electron paramagnetic resonance (EPR) spectra were recorded on a Bruker A300 spectrometer operated in the X-band frequency range at 100 K. The as-synthesized samples were loaded in

EPR tubes and operated with a microwave power of 2.18 mW, modulation frequency of 100 kHz, microwave frequency of 9.33 GHz and modulation amplitude of 1.00 G.

The surface areas were collected at an analyzer (Micromeritics, ASAP 2020, USA). All corresponding samples were degassed at 200 °C for 4 h before the measurement.

X-ray photoelectron spectroscopy (XPS) was characterized by a US Thermo Fisher Scientific ESCALAB Xi+ with Al K α (1486.6 eV) as the excitation source, and the binding energies were corrected by the C1s line at 284.6 eV.

X-ray diffraction (XRD) patterns were obtained on an X-ray diffractometer (Bruker D8 Advance, Germany) with Cu K α radiation, in the 2 θ range from 20 to 80°. Visible Raman spectroscopy was collected on a LabRAMHR evolution laser Raman spectrometer (HORIBA, France), which was equipped with a HeNe laser (532 nm) and a CCD detector. The wavenumber region was in the range of 200–800 cm⁻¹.

Hydrogen temperature-programmed reduction (H₂-TPR) of the calcined sample (100 mg) was carried out on an automated chemisorption analyzer (AutoChem II2920, Micromeritics) equipped with a TCD detector. The sample was firstly pretreated in Ar at 300 °C for 1 h and then cooled down to 50 °C in Ar. After that, the baseline was recorded in 5 vol.% H₂/Ar at a flow rate of 30 mL·min⁻¹ until it was stable. Finally, the sample was heated from 50 to 800 °C at a ramping rate of 5 °C·min⁻¹.

CO₂ temperature-programmed desorption (CO₂-TPD) was conducted on the automated chemisorption analyzer. The calcined catalysts (200 mg) were reduced at 300 °C for 3 h in 5 vol.% H₂/Ar with a flow rate of 30 mL·min⁻¹ and ramping rate of 5 °C·min⁻¹. After cooling down to 45 °C in He, the catalysts were saturated with 20 vol.% CO₂/Ar for 1 h. The CO₂ desorption was recorded by on-line mass spectrometer from 45 to 800 °C in He with a flow rate of 30 mL·min⁻¹.

3.3. Catalytic Activity Test

Catalytic activity test was carried out in a quartz tube reactor (quartz U-tube, 4 mm inner diameter) under atmosphere pressure. The catalysts (200 mg, 40–60 mesh) were loaded into the reactor and pretreated in 5 vol.% H₂/Ar at 300 °C for 3 h prior to the reaction test. Afterwards, the catalysts were flushed with feed gas CO₂/H₂ (1:3 molar ratio, 30 mL·min⁻¹). The reaction was evaluated in the temperature range of 450 to 600 °C, and the products were analyzed by an online gas chromatography. The CO₂ conversion and CO selectivity were defined as follows:

$$X_{\text{CO}_2}(\%) = \frac{N_{\text{CO}_2}^{\text{in}} - N_{\text{CO}_2}^{\text{out}}}{N_{\text{CO}_2}^{\text{in}}} \times 100 \quad (1)$$

$$S_{\text{CO}}(\%) = \frac{N_{\text{CO}}^{\text{out}}}{N_{\text{CO}}^{\text{out}} + N_{\text{CH}_4}^{\text{out}}} \times 100 \quad (2)$$

where $N_{\text{CO}_2}^{\text{in}}$ is corresponded to the concentration of CO₂ in the feed. $N_{\text{CO}_2}^{\text{out}}$, $N_{\text{CO}}^{\text{out}}$ and $N_{\text{CH}_4}^{\text{out}}$ represent the concentrations of CO₂, CO and CH₄ in the outlet gas, respectively.

Additionally, the CO formation rate was defined as follow:

$$R_W = \frac{X_{\text{CO}_2} \times F_{\text{CO}_2} \times S_{\text{CO}}}{m} \quad (3)$$

$$R_{\text{SSA}} = \frac{X_{\text{CO}_2} \times F_{\text{CO}_2} \times S_{\text{CO}}}{m \times S_{\text{SSA}}} \quad (4)$$

where R_W and R_{SSA} is the CO formation rate according to catalyst weight ($\mu\text{mol}\cdot\text{g}^{-1}\cdot\text{s}^{-1}$) and specific surface area ($\mu\text{mol}\cdot\text{m}^{-2}\cdot\text{s}^{-1}$), respectively. m is the mass of the catalysts used (g), S_{SSA} is the specific surface area ($\text{m}^2\cdot\text{g}^{-1}$) and F_{CO_2} is corresponded to the molar flow rate of CO₂ ($\text{mol}\cdot\text{s}^{-1}$).

4. Conclusions

A series of Cu doped ZnO model catalysts were designed and successfully prepared to simulate the direct contact Cu-ZnO interface of the supported Cu-ZnO based catalysts, while the 1Cu/ZnO model catalyst was prepared to simulate both direct contact Cu-ZnO and ZnOx-Cu NP-ZnO interfaces. The comparative investigation indicates that the RWGS reaction reactivity on the direct contact Cu-ZnO interface was inferior to that of the ZnOx-Cu NP-ZnO interface at a temperature lower than 500 °C; however, it is more stable at a reaction temperature higher than 500 °C, which enables ZnO:XCu model catalysts superior catalytic activity to that of 1Cu/ZnO. Considering the typical reaction temperature (200–300 °C) of CO₂ hydrogenation to methanol, both direct contact Cu-ZnO and ZnOx-Cu NP-ZnO interfaces will facilitate CO formation while the latter plays vital roles. Then, the reactivity of CO hydrogenation to methanol on both interfaces will be further investigated in order to elucidate the methanol formation during CO₂ hydrogenation to methanol over Cu-ZnO based catalysts. This finding will help to design more efficient and stable catalysts for both the RWGS reaction and methanol production from CO₂ hydrogenation.

Supplementary Materials: The following are available online at <http://www.mdpi.com/2073-4344/10/5/533/s1>, Figure S1: SEM images of pristine plate ZnO (a) and 1Cu/ZnO (b) after reduction. Figure S2: XRD patterns of ZnO:XCu model catalysts after H₂ reduction, X = 0.5, 1.0, 1.5, 3.5, 6.5. Figure S3: The correlation of the intensity ratio of E₁(LO) to E₂^{high} and the Cu doping content. Figure S4: Raman spectra of the reduced pristine ZnO and ZnO:XCu model catalysts, X = 0.5, 1, 1.5, 3.5, 6.5. Figure S5: H₂-TPD profile of pristine ZnO plate after reduction in H₂ without H₂ adsorption (detected by MS). Figure S6: H₂-TPD profile of plate ZnO:1Cu model catalyst after reduction in H₂ without H₂ adsorption (a) and with H₂ adsorption (b), detected by TCD detector. Figure S7: CO₂-TPD profiles of the 1Cu/ZnO model catalyst. Figure S8: SEM image of ZnO:1Cu model catalyst after RWGS stability evaluation. Table S1: The intensity ratios of E₁(LO) to E₂^{high} and wavenumber of E₂^{high} for the reduced pristine ZnO and ZnO:XCu model catalysts. Table S2: Specific surface area of calcined ZnO and Cu-ZnO model catalysts. Table S3: Surface compositional analysis of ZnO:1Cu model catalyst based on XPS experiment.

Author Contributions: J.W. (Jinjun Wen) planned and carried out the experiments; C.H., Y.Z. (Yujun Zhang) and Y.S. performed the experimental work; L.L. and Y.Z. (Yudong Zhang) contributed to part data analysis; J.W. (Jinjun Wen) wrote the manuscript; M.F., J.W. (Junliang Wu) and D.Y. revised the manuscript; L.C. designed, supervised the project and revised the manuscript. All authors have given approval for the final version of manuscript.

Funding: This work is financially supported by the National Natural Science Foundation of China (No. 21976059, 91645119, 51878292), the Natural Science Foundation of Guangdong Province, China (Grant No. 2019A1515011849), Guangzhou Science and Technology Plan (201607010095) and State Key Laboratory of Physical Chemistry of Solid Surfaces, Xiamen University (No. 201602).

Conflicts of Interest: The authors declare no conflict of interest.

References

1. Huang, C.-H.; Tan, C.-S. A review: CO₂ utilization. *Aerosol Air Qual. Res.* **2014**, *14*, 480–499. [[CrossRef](#)]
2. Song, C. Global challenges and strategies for control, conversion and utilization of CO₂ for sustainable development involving energy, catalysis, adsorption and chemical processing. *Catal. Today* **2006**, *115*, 2–32. [[CrossRef](#)]
3. Khatib, H. IEA world energy outlook 2011—A comment. *Energy Policy* **2012**, *48*, 737–743. [[CrossRef](#)]
4. Aresta, M.; Dibenedetto, A.; Angelini, A. Catalysis for the valorization of exhaust carbon: From CO₂ to chemicals, materials, and fuels. Technological use of CO₂. *Chem. Rev.* **2013**, *114*, 1709–1742. [[CrossRef](#)] [[PubMed](#)]
5. Zheng, Y.; Zhang, W.; Li, Y.; Chen, J.; Yu, B.; Wang, J.; Zhang, L.; Zhang, J. Energy related CO₂ conversion and utilization: Advanced materials/nanomaterials, reaction mechanisms and technologies. *Nano Energy* **2017**, *40*, 512–539. [[CrossRef](#)]
6. Zhang, B.; Chen, Y.; Li, J.; Pippel, E.; Yang, H.; Gao, Z.; Qin, Y. High efficiency Cu-ZnO hydrogenation catalyst: The tailoring of Cu-ZnO interface sites by molecular layer deposition. *ACS Catal.* **2015**, *5*, 5567–5573. [[CrossRef](#)]

7. Behrens, M.; Studt, F.; Kasatkin, I.; Kühl, S.; Hävecker, M.; Abild-Pedersen, F.; Zander, S.; Girgsdies, F.; Kurr, P.; Knief, B.-L. The active site of methanol synthesis over Cu/ZnO/Al₂O₃ industrial catalysts. *Science* **2012**, *336*, 893–897. [[CrossRef](#)]
8. Martinez-Suarez, L.; Siemer, N.; Frenzel, J.; Marx, D. Reaction network of methanol synthesis over Cu/ZnO nanocatalysts. *ACS Catal.* **2015**, *5*, 4201–4218. [[CrossRef](#)]
9. Galván, C.Á.; Schumann, J.; Behrens, M.; Fierro, J.L.G.; Schlögl, R.; Frei, E. Reverse water-gas shift reaction at the Cu/ZnO interface: Influence of the Cu/Zn ratio on structure-activity correlations. *Appl. Catal. B* **2016**, *195*, 104–111. [[CrossRef](#)]
10. Wang, Y.; Gao, W.; Li, K.; Zheng, Y.; Xie, Z.; Na, W.; Chen, J.G.; Wang, H. Strong Evidence of the Role of H₂O in Affecting Methanol Selectivity from CO₂ Hydrogenation over Cu-ZnO-ZrO₂. *Chem* **2020**, *6*, 419–430. [[CrossRef](#)]
11. Lloyd, L.; Ridler, D.; Twigg, M. *Catalyst Handbook*; CRC Press: Boca Raton, FL, USA, 1989; p. 283.
12. Lunkenbein, T.; Schumann, J.; Behrens, M.; Schlögl, R.; Willinger, M.G. Formation of a ZnO overlayer in industrial Cu/ZnO/Al₂O₃ catalysts induced by strong metal–support interactions. *Angew. Chem. Int. Ed.* **2015**, *54*, 4544–4548. [[CrossRef](#)] [[PubMed](#)]
13. Le Valant, A.; Comminges, C.; Tisseraud, C.; Canaff, C.; Pinard, L.; Pouilloux, Y. The Cu–ZnO synergy in methanol synthesis from CO₂, Part 1: Origin of active site explained by experimental studies and a sphere contact quantification model on Cu+ZnO mechanical mixtures. *J. Catal.* **2015**, *324*, 41–49. [[CrossRef](#)]
14. Tisseraud, C.; Comminges, C.; Belin, T.; Ahouari, H.; Soualah, A.; Pouilloux, Y.; Le Valant, A. The Cu–ZnO synergy in methanol synthesis from CO₂, Part 2: Origin of the methanol and CO selectivities explained by experimental studies and a sphere contact quantification model in randomly packed binary mixtures on Cu–ZnO coprecipitate catalysts. *J. Catal.* **2015**, *330*, 533–544. [[CrossRef](#)]
15. Natesakhawat, S.; Lekse, J.W.; Baltrus, J.P.; Ohodnicki, P.R., Jr.; Howard, B.H.; Deng, X.; Matranga, C. Active sites and structure–activity relationships of copper-based catalysts for carbon dioxide hydrogenation to methanol. *ACS Catal.* **2012**, *2*, 1667–1676. [[CrossRef](#)]
16. Witoon, T.; Kachaban, N.; Donphai, W.; Kidkhunthod, P.; Faungnawakij, K.; Chareonpanich, M.; Limtrakul, J. Tuning of catalytic CO₂ hydrogenation by changing composition of CuO–ZnO–ZrO₂ catalysts. *Energy Convers. Manag.* **2016**, *118*, 21–31. [[CrossRef](#)]
17. Liao, F.; Huang, Y.; Ge, J.; Zheng, W.; Tedsree, K.; Collier, P.; Hong, X.; Tsang, S.C. Morphology-Dependent Interactions of ZnO with Cu Nanoparticles at the Materials’ Interface in Selective Hydrogenation of CO₂ to CH₃OH. *Angew. Chem. Int. Ed.* **2011**, *50*, 2162–2165. [[CrossRef](#)]
18. Grunwaldt, J.-D.; Molenbroek, A.; Topsøe, N.-Y.; Topsøe, H.; Clausen, B. In situ investigations of structural changes in Cu/ZnO catalysts. *J. Catal.* **2000**, *194*, 452–460. [[CrossRef](#)]
19. Kattel, S.; Liu, P.; Chen, J.G. Tuning selectivity of CO₂ hydrogenation reactions at the metal/oxide interface. *J. Am. Chem. Soc.* **2017**, *139*, 9739–9754. [[CrossRef](#)]
20. Li, C.; Yuan, X.; Fujimoto, K. Development of highly stable catalyst for methanol synthesis from carbon dioxide. *Appl. Catal. A* **2014**, *469*, 306–311. [[CrossRef](#)]
21. Tisseraud, C.; Comminges, C.; Pronier, S.; Pouilloux, Y.; Le Valant, A. The Cu–ZnO synergy in methanol synthesis Part 3: Impact of the composition of a selective Cu@ ZnOx core–shell catalyst on methanol rate explained by experimental studies and a concentric spheres model. *J. Catal.* **2016**, *343*, 106–114. [[CrossRef](#)]
22. Kuld, S.; Thorhauge, M.; Falsig, H.; Elkjær, C.F.; Helveg, S.; Chorkendorff, I.; Sehested, J. Quantifying the promotion of Cu catalysts by ZnO for methanol synthesis. *Science* **2016**, *352*, 969–974. [[CrossRef](#)] [[PubMed](#)]
23. Kattel, S.; Ramírez, P.J.; Chen, J.G.; Rodriguez, J.A.; Liu, P. Active sites for CO₂ hydrogenation to methanol on Cu/ZnO catalysts. *Science* **2017**, *355*, 1296–1299. [[CrossRef](#)] [[PubMed](#)]
24. Campbell, C.T.; Daube, K.A.; White, J. Cu/ZnO (0001) and ZnOx/Cu (111): Model catalysts for methanol synthesis. *Surf. Sci.* **1987**, *182*, 458–476. [[CrossRef](#)]
25. Palomino, R.M.; Ramírez, P.J.; Liu, Z.; Hamlyn, R.; Waluyo, I.; Mahapatra, M.; Orozco, I.; Hunt, A.; Simonovis, J.P.; Senanayake, S.D. Hydrogenation of CO₂ on ZnO/Cu (100) and ZnO/Cu (111) Catalysts: Role of Copper Structure and Metal–Oxide Interface in Methanol Synthesis. *J. Phys. Chem. B* **2017**, *122*, 794–800. [[CrossRef](#)] [[PubMed](#)]
26. Huang, C.; Wen, J.; Sun, Y.; Zhang, M.; Bao, Y.; Zhang, Y.; Liang, L.; Fu, M.; Wu, J.; Ye, D.; et al. CO₂ hydrogenation to methanol over Cu/ZnO plate model catalyst: Effects of reducing gas induced Cu nanoparticle morphology. *Chem. Eng. J.* **2019**, *374*, 221–230. [[CrossRef](#)]

27. Sun, Y.; Huang, C.; Chen, L.; Zhang, Y.; Fu, M.; Wu, J.; Ye, D. Active site structure study of Cu/Plate ZnO model catalysts for CO₂ hydrogenation to methanol under the real reaction conditions. *J. CO₂ Util.* **2020**, *37*, 55–64. [[CrossRef](#)]
28. Chen, L. Controllable Synthesis Method of Novel Disc-Shaped Zinc Oxide Doped with Transition Metals or Rare Earth Metals. Patent ZL 201610559571.8, 18 June 2019.
29. Bohle, D.S.; Spina, C.J. Controlled Co (II) doping of zinc oxide nanocrystals. *J. Phys. Chem. C* **2010**, *114*, 18139–18145. [[CrossRef](#)]
30. Chakraborti, D.; Narayan, J.; Prater, J. Room temperature ferromagnetism in Zn_{1-x}Cu_xO thin films. *Appl. Phys. Lett.* **2007**, *90*, 062504. [[CrossRef](#)]
31. Xu, H.; Liu, Y.; Xu, C.; Liu, Y.; Shao, C.; Mu, R. Structural, optical, and magnetic properties of Mn-doped ZnO thin film. *J. Chem. Phys.* **2006**, *124*, 074707. [[CrossRef](#)] [[PubMed](#)]
32. Li, D.; Leung, Y.H.; Djurišić, A.B.; Liu, Z.T.; Xie, M.H.; Shi, S.L.; Xu, S.J.; Chan, W.K. Different origins of visible luminescence in ZnO nanostructures fabricated by the chemical and evaporation methods. *Appl. Phys. Lett.* **2004**, *85*, 1601–1603. [[CrossRef](#)]
33. Kakazey, N.; Sreckovic, T.; Ristic, M. Electronic paramagnetic resonance investigation of the evolution of defects in zinc oxide during tribophysical activation. *J. Mater. Sci.* **1997**, *32*, 4619–4622. [[CrossRef](#)]
34. Djurišić, A.B.; Choy, W.C.; Roy, V.A.L.; Leung, Y.H.; Kwong, C.Y.; Cheah, K.W.; Gundu Rao, T.; Chan, W.K.; Fei Lui, H.; Surya, C. Photoluminescence and electron paramagnetic resonance of ZnO tetrapod structures. *Adv. Funct. Mater.* **2004**, *14*, 856–864. [[CrossRef](#)]
35. Alnoor, H.; Savoyant, A.; Liu, X.; Pozina, G.; Willander, M.; Nur, O. An effective low-temperature solution synthesis of Co-doped [0001]-oriented ZnO nanorods. *J. Appl. Phys.* **2017**, *121*, 215102. [[CrossRef](#)]
36. Xue, J.; Wang, X.; Qi, G.; Wang, J.; Shen, M.; Li, W. Characterization of copper species over Cu/SAPO-34 in selective catalytic reduction of NO_x with ammonia: Relationships between active Cu sites and de-NO_x performance at low temperature. *J. Catal.* **2013**, *297*, 56–64. [[CrossRef](#)]
37. Li, G.; Dimitrijevic, N.M.; Chen, L.; Rajh, T.; Gray, K.A. Role of surface/interfacial Cu²⁺ sites in the photocatalytic activity of coupled CuO–TiO₂ nanocomposites. *J. Phys. Chem. C* **2008**, *112*, 19040–19044. [[CrossRef](#)]
38. He, H.; Guo, J.; Xie, X.; Peng, J. Location and migration of cations in Cu²⁺-adsorbed montmorillonite. *Environ. Int.* **2001**, *26*, 347–352. [[CrossRef](#)]
39. Dietz, R.; Kamimura, H.; Sturge, M.; Yariv, A. Electronic structure of copper impurities in ZnO. *Phys. Rev.* **1963**, *132*, 1559. [[CrossRef](#)]
40. Vreugdenhil, W.; Haasnoot, J.G.; Kahn, O.; Thuery, P.; Reedijk, J. A copper (II) dope as a detector for the high-spin. tautm. low-spin transition in the two-dimensional compound [trans-bis (thiocyanato) bis (4, 4'-bi-1, 2, 4-triazole) iron] hydrate. *J. Am. Chem. Soc.* **1987**, *109*, 5272–5273. [[CrossRef](#)]
41. Sambasivam, S.; Sathyaseelan, B.; Reddy, D.R.; Reddy, B.; Jayasankar, C. ESR and photoluminescence properties of Cu doped ZnS nanoparticles. *Spectrochim. Acta A* **2008**, *71*, 1503–1506. [[CrossRef](#)]
42. Gervasini, A.; Manzoli, M.; Martra, G.; Ponti, A.; Ravasio, N.; Sordelli, L.; Zaccheria, F. Dependence of copper species on the nature of the support for dispersed CuO catalysts. *J. Phys. Chem. B* **2006**, *110*, 7851–7861. [[CrossRef](#)]
43. Kivelson, D.; Neiman, R. ESR studies on the bonding in copper complexes. *J. Chem. Phys.* **1961**, *35*, 149–155. [[CrossRef](#)]
44. Sushkevich, V.L.; van Bokhoven, J.A. Revisiting copper reduction in zeolites: The impact of autoreduction and sample synthesis procedure. *Chem. Commun.* **2018**, *54*, 7447–7450. [[CrossRef](#)] [[PubMed](#)]
45. Drmosh, Q.A.; Rao, S.G.; Yamani, Z.H.; Gondal, M.A. Crystalline nanostructured Cu doped ZnO thin films grown at room temperature by pulsed laser deposition technique and their characterization. *Appl. Surf. Sci.* **2013**, *270*, 104–108. [[CrossRef](#)]
46. Peng, X.; Xu, J.; Zang, H.; Wang, B.; Wang, Z. Structural and PL properties of Cu-doped ZnO films. *J. Lumin.* **2008**, *128*, 297–300. [[CrossRef](#)]
47. Šćepanović, M.; Grujić-Brojčin, M.; Vojisavljević, K.; Bernik, S.; Srećković, T. Raman study of structural disorder in ZnO nanopowders. *J. Raman Spectrosc.* **2010**, *41*, 914–921. [[CrossRef](#)]
48. Wang, X.; Xu, J.; Zhang, B.; Yu, H.; Wang, J.; Zhang, X.; Yu, J.; Li, Q. Signature of intrinsic high-temperature ferromagnetism in cobalt-doped zinc oxide nanocrystals. *Adv. Mater.* **2006**, *18*, 2476–2480. [[CrossRef](#)]

49. Rajalakshmi, M.; Arora, A.K.; Bendre, B.; Mahamuni, S. Optical phonon confinement in zinc oxide nanoparticles. *J. Appl. Phys.* **2000**, *87*, 2445–2448. [[CrossRef](#)]
50. Reddy, G.K.; Gunasekera, K.; Boolchand, P.; Dong, J.; Smirniotis, P.G. High temperature water gas shift reaction over nanocrystalline copper codoped-modified ferrites. *J. Phys. Chem. C* **2011**, *115*, 7586–7595. [[CrossRef](#)]
51. Schumann, J.; Eichelbaum, M.; Lunkenbein, T.; Thomas, N.; Alvarez Galvan, M.C.; Schlögl, R.; Behrens, M. Promoting strong metal support interaction: Doping ZnO for enhanced activity of Cu/ZnO: M (M = Al, Ga, Mg) catalysts. *ACS Catal.* **2015**, *5*, 3260–3270. [[CrossRef](#)]
52. Chen, L.; Wang, J.; Valenzuela, M.; Bokhimi, X.; Acosta, D.; Novaro, O. Hydrogen spillover and structural defects in a PdO/zirconia nanophase synthesized through a surfactant-templated route. *J. Alloy. Compd.* **2006**, *417*, 220–223. [[CrossRef](#)]
53. Dong, X.; Li, F.; Zhao, N.; Xiao, F.; Wang, J.; Tan, Y. CO₂ hydrogenation to methanol over Cu/ZnO/ZrO₂ catalysts prepared by precipitation-reduction method. *Appl. Catal. B* **2016**, *191*, 8–17. [[CrossRef](#)]
54. Huang, C.; Chen, S.; Fei, X.; Liu, D.; Zhang, Y. Catalytic hydrogenation of CO₂ to methanol: Study of synergistic effect on adsorption properties of CO₂ and H₂ in CuO/ZnO/ZrO₂ system. *Catalysts* **2015**, *5*, 1846–1861. [[CrossRef](#)]
55. Thang, H.V.; Pacchioni, G. Electronic structure of Al, Ga, In and Cu doped ZnO/Cu (111) bilayer films. *Phys. Chem. Chem. Phys.* **2019**, *21*, 369–377. [[CrossRef](#)] [[PubMed](#)]
56. Liu, P.; Derchi, M.; Hensen, E.J. Promotional effect of transition metal doping on the basicity and activity of calcined hydrotalcite catalysts for glycerol carbonate synthesis. *Appl. Catal. B* **2014**, *144*, 135–143. [[CrossRef](#)]
57. Cantrell, D.G.; Gillie, L.J.; Lee, A.F.; Wilson, K. Structure-reactivity correlations in MgAl hydrotalcite catalysts for biodiesel synthesis. *Appl. Catal. A* **2005**, *287*, 183–190. [[CrossRef](#)]
58. Di Cosimo, J.; Diez, V.; Xu, M.; Iglesia, E.; Apesteguia, C. Structure and surface and catalytic properties of Mg-Al basic oxides. *J. Catal.* **1998**, *178*, 499–510. [[CrossRef](#)]
59. Yue, H.; Zhao, Y.; Zhao, S.; Wang, B.; Ma, X.; Gong, J. A copper-phyllsilicate core-sheath nanoreactor for carbon–oxygen hydrogenolysis reactions. *Nat. Commun.* **2013**, *4*, 2339. [[CrossRef](#)]
60. Prieto, G.; Zečević, J.; Friedrich, H.; De Jong, K.P.; De Jongh, P.E. Towards stable catalysts by controlling collective properties of supported metal nanoparticles. *Nat. Mater.* **2013**, *12*, 34. [[CrossRef](#)]



© 2020 by the authors. Licensee MDPI, Basel, Switzerland. This article is an open access article distributed under the terms and conditions of the Creative Commons Attribution (CC BY) license (<http://creativecommons.org/licenses/by/4.0/>).